Nucleic Acids Research, 2023, 1–12
https://doi.org/10.1093/nar/gkad808
Nucleic Acid Enzymes

Impact of bound ssRNA length on allostery in the Dengue Virus NS3 helicase

Fernando Amrein[1,4,†], **Carolina Sarto**[2,4,†], **Leila A. Cababie**[1], **F. Luis Gonzalez Flecha**[1,3], **Sergio B. Kaufman**[1,3] and **Mehrnoosh Arrar**[4,*]

[1]Universidad de Buenos Aires, CONICET, Instituto de Química y Fisicoquímica Biológicas (IQUIFIB), Junín 956, CABA 1113, Argentina
[2]Universidad de Buenos Aires, CONICET, Instituto de Química Biológica de la Facultad de Ciencias Exactas y Naturales (IQUIBICEN), Intendente Guiraldes 2160, CABA 1428, Argentina
[3]Universidad de Buenos Aires, Departamento de Química Biológica, Facultad de Farmacia y Bioquímica, Junín 956, CABA 1113, Argentina
[4]Universidad de Buenos Aires, CONICET, Instituto de Cálculo, Intendente Guiraldes 2160, CABA 1428, Argentina

[*]To whom correspondence should be addressed. Email: marrar@ic.fcen.uba.ar
[†]Contributed equally to this work.

Abstract

The presence of ATP is known to stimulate helicase activity of the Dengue Virus Non-structural protein 3 helicase (NS3h), and the presence of RNA stimulates NS3h ATPase activity, however this coupling is still mechanistically unclear. Here we use atomistic models and molecular dynamics simulations to evaluate the single-stranded RNA (ssRNA)-length dependence of the NS3h–ssRNA binding affinity and its modulation by bound ATP. Considering complexes with 7, 11, 16 and 26 nucleotides (nts), we observe that both the binding affinity and its modulation by bound ATP are augmented with increased ssRNA lengths. In models with at least 11 nts bound, the binding of ATP results in a shift from a tightly bound to a weakly bound state. We find that the weakly bound state persists during both the ADP-Pi- and ADP-bound stages of the catalytic cycle. We obtain the equilibrium association constants for NS3h binding to an ssRNA 10-mer *in vitro*, both in the absence and presence of ADP, which further support the alternation between tightly and weakly bound states during the catalytic cycle. The length of bound ssRNA is critical for understanding the NS3h–RNA interaction as well as how it is modulated during the catalytic cycle.

Graphical abstract

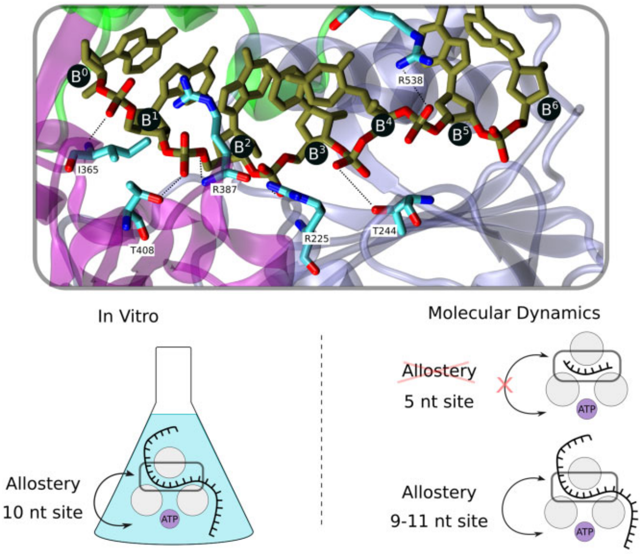

Introduction

The Dengue virus (DENV) is the cause of Dengue fever, a mosquito-borne disease that is a global public health concern. Dengue fever is prevalent in South America, India and Southeast Asia, although the area of influence of the disease is expected to increase due to climate changes that favor the proliferation of the vector species (*A. aegypti* and *A. albopictus*) (1). Despite recent strides in vaccine development, an effective vaccine is not yet widely available (2), making the develop-

Received: March 9, 2023. **Revised:** August 20, 2023. **Editorial Decision:** September 13, 2023. **Accepted:** September 19, 2023

ment of novel antiviral therapies of particular interest in the affected countries (3).

Non-structural protein 3 (NS3) is one such potential antiviral drug target as it is a multifunctional protein that is critical (4) in the DENV life cycle. NS3 is involved in viral replication, encapsidation, host immune evasion and processing of the polyprotein precursor (5,6). NS3 consists of an N-terminal serine protease domain (residues 1 to 169) connected via a flexible linker to a C-terminal helicase domain (residues 179 to 618) (Figure 1a). Despite its name, the C-terminal helicase domain of NS3 (NS3h) also functions as an NTPase, RTPase and possesses RNA annealing activities (7–10). Importantly, these activities are retained to an extent even in recombinant NS3h isolated from the N-terminal protease domain (4,11,12).

Even though NS3h performs multiple functions, here we will focus on its role as an energy transducer or molecular motor that translocates along single-stranded and unwinds double-stranded RNA in a 3′-to-5′ direction while catalyzing the hydrolysis of nucleoside triphosphates (NTPs). The NTPase and helicase activities of the DENV NS3h are coupled such that the hydrolysis of NTPs is necessary for the translocation along a strand of RNA or the unwinding of double-stranded RNA (12). Crystallographic studies of the DENV NS3h have shed substantial light on our understanding of the physical mechanisms that underlie the coupled NTPase and helicase activities (13,14). NS3h recognition of single stranded RNA (ssRNA) is known to be sequence independent (15) and crystal structures of NS3h in absence and presence of RNA have depicted that the NTPase catalytic site adopts a hydrolysis-competent conformation in presence of RNA. This conformational change has been proposed to be key in the RNA-stimulated NTPase activity (12).

Crystallographic structures of NS3h bound to ssRNA reveal only subtle conformational changes during the NTPase catalytic cycle (13). This is in sharp contrast to the differences observed in the crystallographic snapshots obtained for the hepatitis C virus (HCV) NS3h, in which clear open and closed conformations could be mechanistically related to the RNA displacement that occurs during the NTPase hydrolysis cycle (16). Even though the communication between the ATP binding site and the RNA binding site within the DENV NS3h is expected, thermodynamic data are still needed to confirm this hypothesis.

In previous work (17), we focused on the ssRNA-bound NS3h structures and used molecular dynamics (MD) simulations to further explore the conformational landscape of NS3h in three stages of the ATP hydrolysis cycle (apo, ATP-bound and ADP-Pi-bound states). In these simulations, we observed a flexible-rigid-flexible alternation in the protein dynamics for the apo, ATP-bound and product-bound stages of the ATP hydrolysis cycle, respectively. Furthermore, we identified a novel open-loop conformation of the $\beta 6$-$\beta 1'$ loop (residues 316 to 330) that forms a backdoor channel to the active site, facilitating the release of Pi, the first product of the ATP hydrolysis (18). Other computational studies of the allostery in the DENV NS3h provided a possible description of the effect of RNA binding on the hydrolysis reaction and proposed that motif V controls the communication between the ATP and RNA binding sites (19,20). Nevertheless, a thermodynamic relationship between the ATPase catalytic site and the RNA binding site has yet to be established.

Interestingly, thermodynamic studies of the binding of the helicase to oligonucleotides of different lengths have been carried out and indicate that the minimum ssRNA binding site size of NS3h is 10-11 nucleotides (nts) (15). Although the available crystal structures of NS3h were obtained in complex with a 12-mer ssRNA, only 7 nucleotides (nts) were resolved (13) and of these 7 nts, only four appear to form stable interactions with the protein.

Here, we test the hypothesis that the RNA binding site size (namely, the number of nucleotides that form the NS3h–ssRNA interface) of the DENV NS3h is indeed greater than the 7 nts resolved in the crystal structures, and ask whether the presence of a longer ssRNA is necessary to observe the interaction between the NTPase and RNA binding sites. To address this question, we modeled the DENV NS3h bound to a 7-, 11-, 16- and 26-mer ssRNA (Figure 1b) and performed MD simulations to examine conformational changes in the protein as well as the relative RNA binding affinity in the presence or absence of ATP. We then use a single ssRNA length (16 -mer) to evaluate how the affinity of NS3h for ssRNA changes in different stages of the ATP hydrolysis cycle (Figure 1c). To evaluate the RNA binding affinity in different stages of the catalytic cycle, we used both molecular mechanics generalized born surface area (MM-GBSA) calculations from MD simulations as well as isothermal titration calorimetry (ITC) and conclude that on binding ATP, the NS3h–ssRNA complex shifts from a tightly bound to a weakly bound state, which is maintained until both products of hydrolysis are released. Together, these results clearly establish an allosteric communication between the ssRNA and ATP binding sites of NS3h. We relate the changes in affinity to conformational changes in the protein that shed light on the physical translocation mechanism.

Materials and methods

System preparation

The DENV NS3h was crystallized bound to a 12-mer fragment of ssRNA with the active site free (PDB ID 2JLU) (13), of which only 7 nts were resolved. Three additional complexes were created using this initial structure (sequence corresponding to DENV 4 serotype (residues 180 to 618)) by adding a total of 4, 9 and 19 nts of adenosine. The nucleotides were added using the program VMD (21) to move copies of existing nucleotides to the corresponding ends of the RNA and saving the coordinates. Thus, four complexes were obtained: a 7-, 11-, 16- and 26-mer ssRNA, each bound to the NS3h with a free active site. For the 11-mer, two adenosines were added to each the 3′ and 5′ termini of the 7-mer in crystal structure, for the 16-mer 4 and 5 adenosines were added to the 3′ and 5′ termini, respectively, and for the 26-mer a total of 9 and 10 adenosines were added to the 3′ and 5′ termini, respectively. For all lengths, both apo and ATP-bound complexes were simulated, while for the 16-mer two additional complexes were simulated: an ADP-Pi-bound system, NS3h bound to ADP and HPO_4^{2-} (Pi) and an ADP-bound system, NS3h bound to only ADP. The ATP-, ADP- and ADP-Pi-bound states were constructed by aligning the respective crystal structures and adding the relevant molecule(s) to the active site (coordinates were taken from the PDB IDs 2JLV, 2JLZ and 2JLY, respectively).

ATP and ADP molecular parameters were obtained from literature (22), while protein residues and ssRNA were modeled with the Amber ff14SB force field using the ILDN correc-

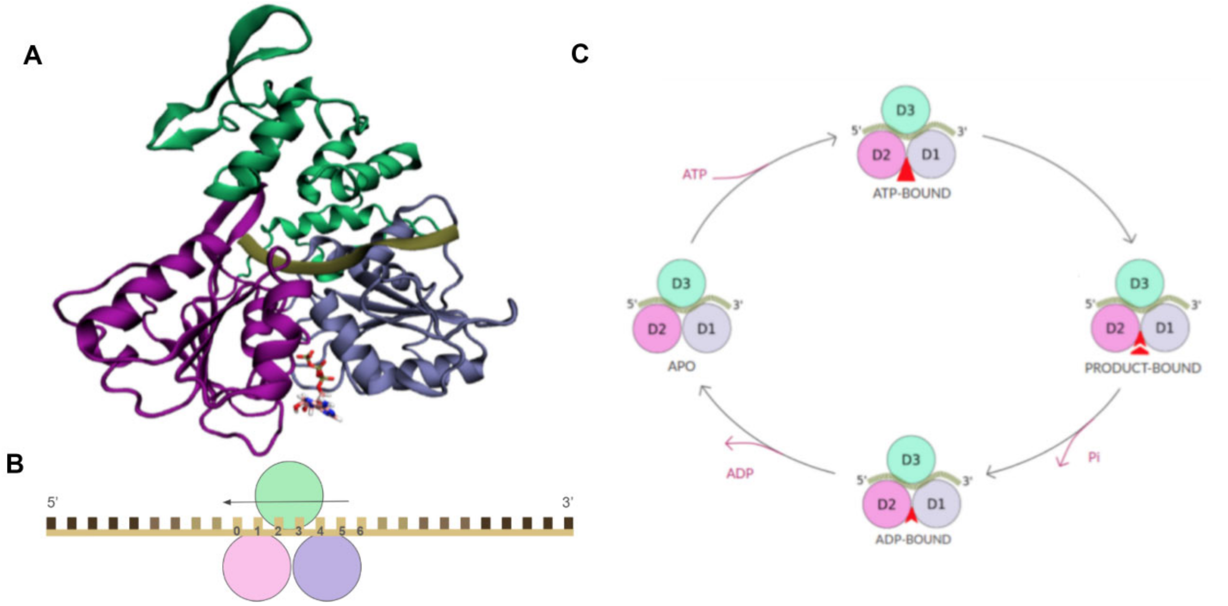

Figure 1. Structural organization of the DENV NS3h and studied complexes. (**A**) Crystal structure of NS3h (PDB ID 2JLV). Subdomains are color-coded with D1 (residues 180 to 329), D2 (residues 330 to 479) and D3 (residues 480 to 618) in purple, magenta and green, respectively. A tan ribbon represents the bound ssRNA, and bound ATP is shown as sticks (Adapted from Sarto *et al.* (17), with permission). (**B**) Schematic representation of the numbering of RNA bases. NS3h subdomains are color-coded as in (**A**). The nucleotides are numbered in the 5′ to 3′ direction according to its corresponding base, with numbers 0 to 6 reserved for the nucleotides resolved in the crystal structure. The gray arrow shows the 3′-to-5′ direction of translocation of the NS3h. (**C**) Schematic diagram of the NS3h ATP hydrolysis cycle, with the apo, ATP-bound, ADP-Pi-bound and ADP-bound complexes labeled.

tion for protein residues and revised RNA dihedral parameters (23,24). Phosphate parameters are the same as described in our previous work (17). Hydrogens and other atoms not resolved in the crystallographic structures were added using the tLeAP module of the Amber simulation suite (25). The protonation states of ionizable residues were also conserved from our previous work (17). The water model used was TIP3P (26). Each system was solvated in an octahedron at 8 Å from the protein–nucleic acid surface, with added TIP3P residues ranging from ∼10 000 in the smaller complexes to ∼100 000 in the larger ones. Ions (Na^+ and Cl^-) were added so that a concentration of 0.15 M of salt was obtained, and so that the total system charge was neutralized.

MD simulations

Three simulations were performed for each system, i.e. different ssRNA lengths and stages of the hydrolysis cycle, totalling 30 independent simulations of 1 μs each (see Table 1 for a more detailed breakdown). Simulations were performed with the PMEMD cuda module of the Amber simulation suite. Each system was heated at constant volume from 0 to 200 K with restraints (100 kcal/mol/$Å^2$ force constant) on the protein backbone during 50 ps, and then weaker restraints were used (50 kcal/mol/$Å^2$) to heat from 200 to 300 K. The system was then equilibrated without restraints for 50 ps, and finally an unrestrained constant-pressure simulation was run to allow volume to fluctuate and density of the solvent to equilibrate during 100 ps with the Berendsen barostat with isotropic position scaling and a pressure relaxation time of 2 ps. Finally three independent replicas were run at constant volume and temperature with the Langevin thermostat for roughly 1 μs with a 2.0-fs timestep, of which the initial 200 ns were discarded from the analysis.

Table 1. Breakdown of simulations performed (three replicas ∼ 1 μs each)

Condition	ssRNA length
apo	7-mer
	11-mer
	16-mer
	26-mer
ATP-bound	7-mer
	11-mer
	16-mer
	26-mer
ADP-Pi-bound	16-mer
ADP-bound	16-mer

MM/GBSA calculations

Frames were saved at 10-ns intervals for each run, discarding the initial 200 ns, from the trajectories of the ssRNA–NS3h complexes, either in presence or absence of ATP. A modified Generalised Born (GB) model developed by A. Onufriev, D. Bashford and D.A. Case was used (Amber flag 'igb' equal to 2) (27) with a salt concentration of 0.15 M.

Isothermal Titration Calorimetry

A construct encoding the helicase domain of NS3 (residues 171–618) was derived from the cDNA of an infected clone of DENV serotype 2 (GenBank accession number U87411) (28). Calorimetric titrations were carried out between NS3h and the ssRNA p-5′-AGUUGAGUUG-3′ (p-R_{10}) in absence and presence of ADP (0.18 M) to obtain binding equilibrium constants that characterize the NS3h–ssRNA interaction in these two states. ITC and spectroscopy experiments were carried out at 25ºC and pH 6.5 in presence of 0.11 M monovalent cations.

Results

Effect of RNA length on NS3h–RNA structural models

NS3h evidences increased conformational flexibility when bound to longer ssRNA

To gauge the ssRNA-length dependence of NS3h flexibility, we calculated the root mean squared deviation (RMSD) of the protein backbone atoms from the crystallographic conformation of NS3h bound to a 7-mer ssRNA (PDB ID 2JLU). Histograms of the RMSD values corresponding to the concatenated three 1-μs simulations are shown in Figure 2 for each of the four ssRNA lengths considered (7, 11, 16 and 26-mers). The histograms indicate a shift toward higher values of RMSD for the NS3h bound to longer ssRNA, suggesting a larger deviation from the crystallographic conformation due to the presence of longer ssRNA. Furthermore, the histograms tend to broaden in states with longer ssRNA, suggesting increased conformational flexibility of the protein backbone on the timescales simulated. In general, the presence of ATP stabilizes the protein conformation (Figure 2, opaque series), as has been reported for other helicases (29,30); nevertheless, even these distributions broaden when longer ssRNA is bound to the protein.

To further explore the deviations from the crystallographic conformation due to the presence of longer ssRNA, we evaluated the per-residue root mean square fluctuation (RMSF) for the backbone atoms (Figure 3a and b). In both the apo and ATP-bound states, we found higher per-residue RMSF values for regions in D3, specifically in two α-helices: α-helix 3″ (526 to 541) and α-helix 7″ (603 to 616), both of which grip the RNA within the binding site. Interestingly, the β5A'-β5B' hairpin that we will refer to as the hydrophobic hairpin (residues 426 to 448) (Figure 3b) evidences increased flexibility in an ssRNA-length-dependent manner. In all cases of extended 11-, 16- and 26-mer ssRNA bound to NS3h, the 5′ end of the modeled RNA wraps around D3, forming new interactions with the protein (Figure 3c).

In all the crystallographic structures of the DENV NS3h the β6-β1′ loop (Figure 3d) is in a single 'closed' conformation. In our previous work (17,18), we showed that this loop can also adopt an open conformation that kinetically favors the release of the first product of the ATP hydrolysis, Pi (18). The open conformation of the β6-β1′ loop was observed in our previous work (17), albeit with low probability (∼10%), in simulations of the apo and product-bound complexes, whereas it remained in the closed-loop conformation in the presence of ATP. In this work, we observed that regardless of the ssRNA length, the presence of ATP stabilizes the closed-loop conformation (Figure 3b). The variation of the oligonucleotide length from 7 to 26 nts does not appear to significantly affect the open-closed conformational equilibrium observed in the 1-μs simulations (Supplementary Figure S1).

Although the 3′ end of the RNA is more flexible (Supplementary Figure S2), it tends to curl for the most part around D1 (Figure 3c). Similar to the trend observed in the flexibility of the 3′ end of the RNA, it is interesting to note that even though the overall flexibility of the protein decreases upon binding ATP (Figure 2), the flexibility of the RNA binding loop (residues 243 to 256), in turn, increases (Figure 3b).

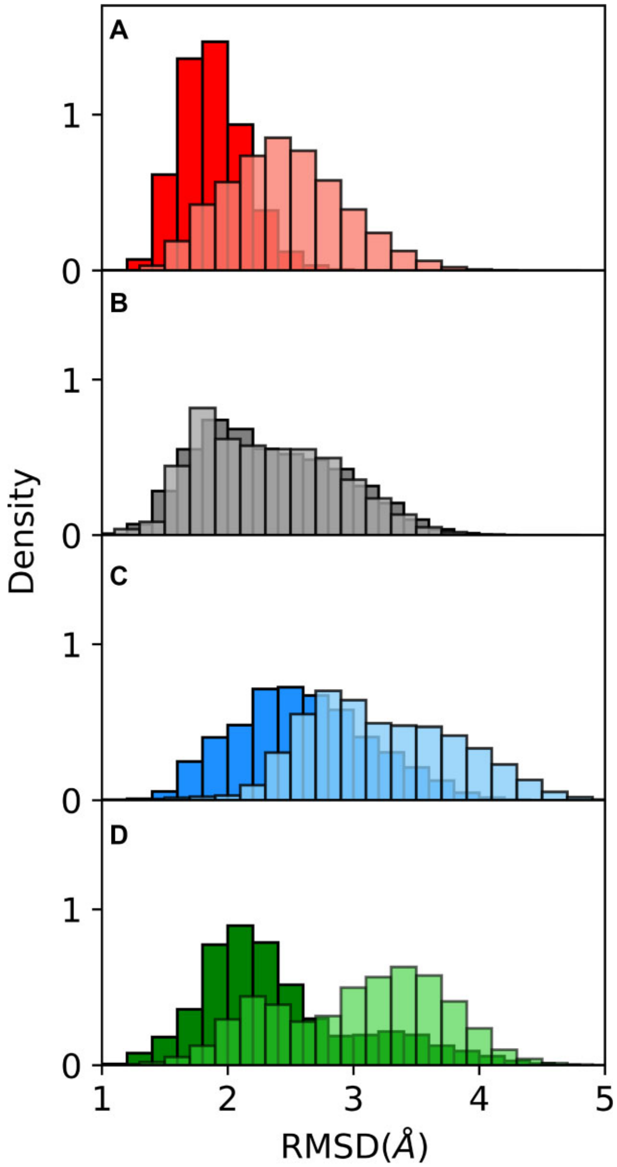

Figure 2. Histograms of protein backbone RMSD from PDB ID 2JLU in simulations of the NS3h bound to **(A)** 7-mer, **(B)** 11-mer, **(C)** 16-mer or **(D)** 26-mer ssRNA. In each panel, transparent and opaque colors represent apo and ATP-bound complexes, respectively.

RNA binding site of NS3h occupies approximately 10 nts

To estimate the RNA binding site size of NS3h, we considered the solvent accessible surface area (SASA) of each nucleotide of the ssRNA fragment, under the assumption that the nucleotides forming part of the RNA binding site are less accessible to solvent molecules. Thus, we selected a certain SASA range as a threshold, and consider nucleotides with SASA below this threshold to be part of the binding site.

The minimum ssRNA binding site size based on *in vitro* experiments has been reported to be ∼10 nts (15). Here, we use the per-nucleotide (per-nt) SASA to map out the RNA binding site size of NS3h bound to ssRNA fragments of increas-

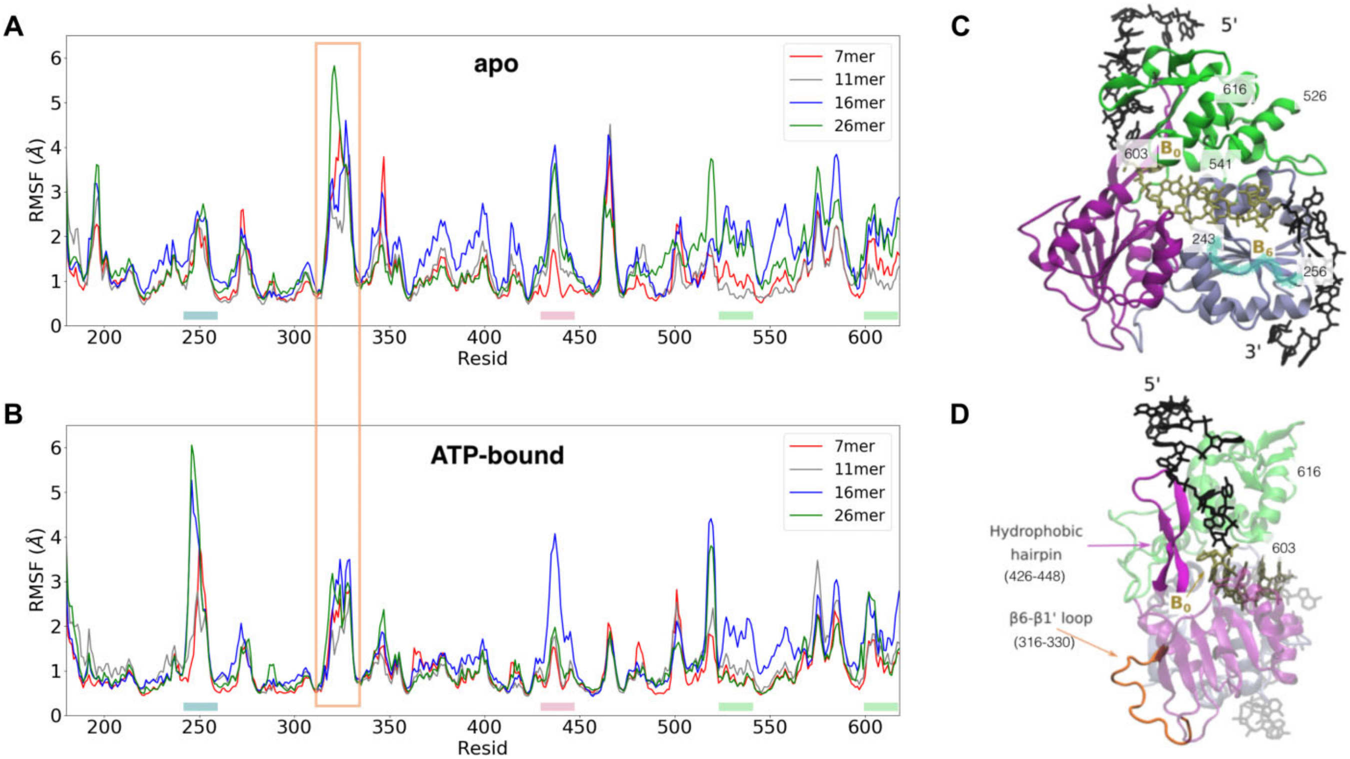

Figure 3. Per-residue RMSF of protein backbone in the **(A)** apo and **(B)** ATP-bound states. Series are colored according to the length of bound ssRNA: 7 (red), 11 (gray), 16 (blue) or 26 nts (green). The orange rectangle indicates the β6-β1′ loop residues. NS3h bound to modeled 26-mer ssRNA is shown in **(C)** with NS3h subdomains colored as in Figure 1. ssRNA is shown as tan sticks for the crystallized nucleotides and black for the extended nucleotides. The 5′ and the 3′ termini of the ssRNA crystallographically resolved (B^0 and B^6, respectively) are labeled as a reference **(D)** NS3h–RNA complex is shown rotated 90° about the vertical axis with respect to panel A. The hydrophobic hairpin is depicted and colored according to its subdomain and the β6-β1′ loop is highlighted in orange. Residue indices highlighted in panels **(A)** and **(B)** at the bottom of each panel are colored accordingly and labeled in panels **(C)** and **(D)**.

ing lengths: 7, 11, 16 and 26 nts (Figure 4, top to bottom), and compare the RNA binding site sizes in the presence and absence of ATP (Figure 4, solid circles and transparent triangles, respectively). The nucleotides are numbered according to its corresponding base as in the scheme in Figure 1b, with the crystallographic 7-mer numbered from 0 to 6 and negative values or values >6 indicating those added to the 5′ or 3′ termini, respectively. From this point on we will use the notation B^x, with x being the base number according to this numbering scheme, to refer to specific positions in the oligonucleotides.

For the 7-mer complex, both of the series of Figure 4a reflects a similar pattern of lower SASA values for B^0 to B^4. Thus, the apparent RNA binding site size in this case is roughly 5 nts, with the bases toward the 3′ terminus being more solvent-exposed, which is consistent with their observed higher flexibility (Supplementary Figure S2). On extending the length of the ssRNA, the adjacent nucleotides adopt stable conformations (Figure 4b-d), increasing the size of the RNA binding site (Table 2). This trend is upheld for the lengths of ssRNA considered here, with an RNA binding site size of 9–11 nts observed for the apo system, which coincides with the reported minimum occluded RNA binding site size determined *in vitro* (15). In contrast to that of the apo complex, the RNA binding site size of the ATP-bound complex is two bases longer at the 3′ end in the 26-mer compared to the 16-mer; however in both cases, the site starts at B^{-2}. An estimation of the RNA site size for NS3h bound to ATP (or an analogue) in bulk has not been reported yet. We obtained comparable results by analyzing the per-nt RMSF, considering nts with low RMSF values as part of the RNA binding site (Supplementary Figure S2). By comparing the distribution of center-of-mass distances between D1 and D2, we were able to discard the possibility that the observed increase in the RNA binding site size may be due to a separation of the two subdomains, and is indeed due to the ssRNA forming new transient interactions with the protein (Supplementary Figure S3).

Table 2. Apparent RNA binding site sizes calculated from per-nt SASA

ssRNA length	Apo Binding site size (nts)	ATP-bound Binding site size (nts)
7-mer	5	5
11-mer	6	5
16-mer	7–11	5–7
26-mer	9–11	9

The apparent RNA binding site sizes estimated from the per-nt SASA analysis with the threshold indicated in Figure 4 are summarized in Table 2 as ranges, where the lower and upper ends of the ranges correspond to the RNA binding site size considering the lower and upper threshold values, respectively (see Supplementary Figure S4 for further analysis on threshold selection). Notably, the size of the RNA binding site does not change significantly between the 16- and 26-mer complexes. We further observe that although the presence of ATP (Figure 4, opaque circles) hardly affects the apparent RNA binding site size in the 7-mer or the 11-mer complexes, it does

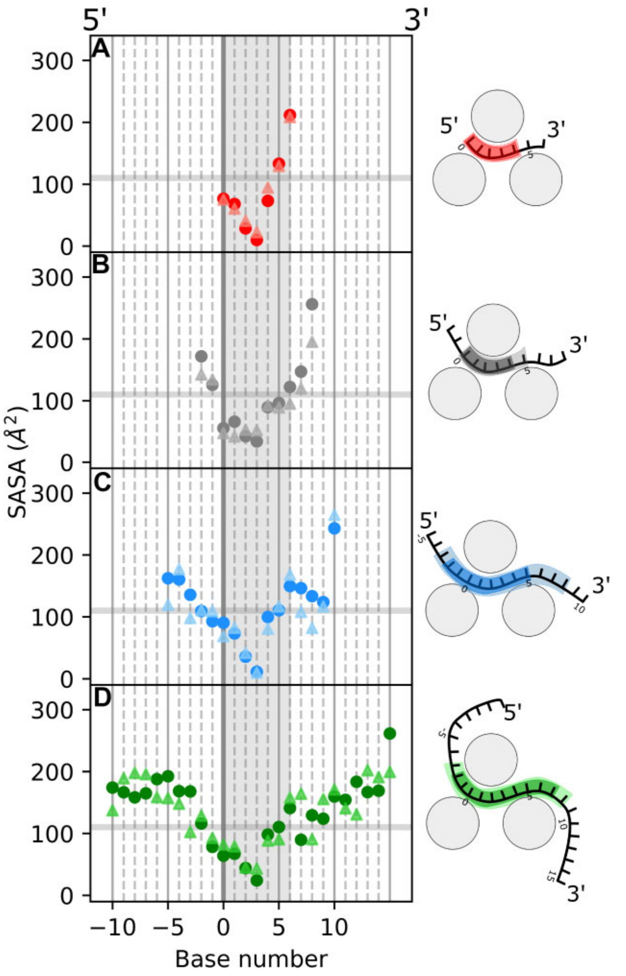

Figure 4. Per-nt solvent accessible surface area (SASA) plots for the **(A)** 7-mer, **(B)** 11-mer, **(C)** 16-mer and **(D)** 26-mer. The lighter, transparent triangle markers and the solid circles correspond to the apo and ATP-bound complexes, respectively. The gray horizontal band indicates a threshold of 105–115 $\AA^2$ used to classify a nucleotide as part of the RNA binding site. The gray shaded vertical region highlights the seven crystallographically resolved nts. Dashed vertical lines for every base and solid vertical lines for every five bases, as well as a thicker, darker line at B^0, have been added for ease of reading. The 5′ and 3′ ends of the ssRNA are labeled at the top of panel A. Additional schematics have been added to the right of the panels for each of the systems.

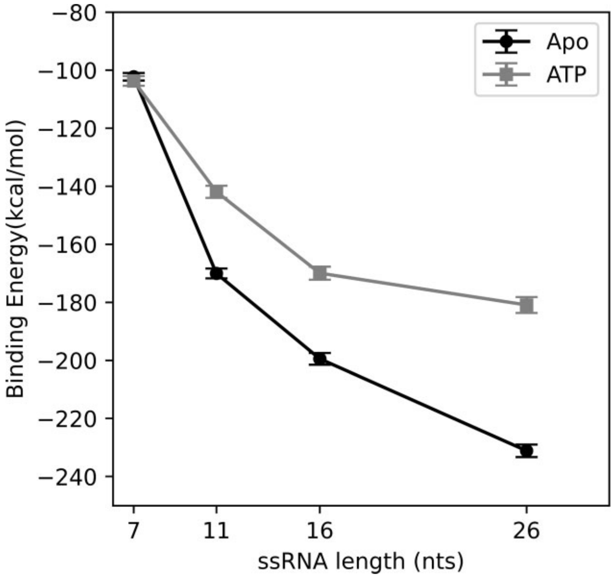

Figure 5. MM-GBSA binding free energy estimates for the apo (black) and ATP-bound (gray) NS3h–RNA complexes, with ssRNA of different lengths. For each state, average values and standard error of the mean were obtained from ∼240 total frames, taken at 10-ns intervals from the last 800 ns of each of the three 1-μs trajectories.

have a noticeable effect in both the 16- and 26-mer systems: in both cases the RNA binding site size is reduced on binding ATP. Again, this observation is independent of the relative D1–D2 orientation, which appears to always adopt a more closed conformation in presence of ATP, regardless of the length of bound ssRNA (Supplementary Figure S3). These results indicate that an oligonucleotide of 16 nts is more adequate than one of 7 or 11 nts in terms of accurately modeling the NS3h–ssRNA binding site size.

Modulation of the NS3h–ssRNA affinity by ATP depends on ssRNA length

To further assess how the NS3h–RNA interaction changes in the presence of a longer oligonucleotide, we estimated the NS3h–RNA binding free energy for each complex using a MM-GBSA approach (Figure 5). The overall NS3h–RNA binding energy decreases as the length of the oligonucleotide increases from 7 to 26 nts, while the per-nt stabilization, represented by the slope, drops with the increase of the ssRNA length, suggesting that the binding energy for the 26-mer complex is approximating a converged length-independent binding free energy (Supplementary Table S1).

The effect of ATP binding is dramatically impacted by the oligonucleotide length. The relative change in RNA binding free energy for the apo and ATP-bound complexes (note the gap between black and gray series in Figure 5 and Supplementary Table S2) is null for the 7-mer, and it becomes more evident as the ssRNA length is increased to 11, 16 and 26 nts. Thus, the presence of ATP results in a weaker NS3h–RNA binding interaction. This would provide evidence of the allostery between the RNA and ATP binding sites, which has only previously been reported in terms of the kinetics of the NTPase activity (8). We further note that the decrease in RNA affinity due to the presence of ATP is similar to the effect reported for the HCV NS3h (31,32). The estimated size of the RNA binding site together with the modulation of RNA affinity by ATP, both observed exclusively for complexes with extended (>10-nt) oligonucleotides, suggest that the transient interactions formed with the extended ssRNA fragments are necessary to accurately model the NS3h–RNA complex.

Conformational and thermodynamic changes during the catalytic cycle

RNA binding site size and NS3h–RNA binding free energy

The analysis of the varying ssRNA lengths considered so far suggests that the RNA binding site size is similar for the 16- and 26-mer complexes (Table 2) and the relative difference in RNA-NS3h binding free energy for apo and ATP-bound complexes is similar for the 11-, 16- and 26-mer complexes (Figure 5). Taking into account the 6-fold increase in computational time required to simulate the 26-mer system compared to the 16-mer, we selected the latter as a representative model with sufficiently long ssRNA bound to further explore the product-bound stages of the ATP hydrolysis cycle.

To analyze the dynamics of the NS3h bound to ssRNA (16-mer) throughout the catalytic cycle, we took a closer look at how the RNA binding site size and NS3h–RNA binding free energy change for the apo, ATP-bound, ADP-Pi-bound and ADP-bound complexes.

In Figure 6a, we show the per-nucleotide SASA values for each of the four stages, with a horizontal band indicating a 105–115 Å^2 threshold used to determine the RNA binding site size of the NS3h. As mentioned earlier, in the apo complex the size of the RNA binding site is ∼10 nts (B^{-3} to B^8), and the presence of ATP in the catalytic site reduces this size by 4 nts (B^{-2} to B^5) (Schematic in Figure 6b). Although the presence of ADP-Pi does not cause an overall change in the RNA binding site size, the site appears to shift slightly toward the 3′ terminus.

On binding ATP, we also note an increase in the flexibility of the 3′ terminus that is retained in both the ADP-Pi-bound and ADP-bound complexes, whereas the 5′ terminus appears to stabilize after hydrolysis and then destabilize again with the release of the first product of the ATP hydrolysis, Pi (per-nt RMSF in Supplementary Figure S5). The increased flexibility of the RNA binding loop on ATP binding is retained in the presence of the products of hydrolysis, but after phosphate release this loop is stabilized again (Supplementary Figure S6).

Using ITC and spectroscopy experiments, we obtained the equilibrium constants for the binding of the NS3h to a 10-mer ssRNA in the absence ($5 \pm 1 \times 10^6$ M^{-1}) and in the presence ($3 \pm 1 \times 10^3$ M^{-1}) of ADP (Figure 6c). These results agree with the existence of the interaction between the NTP and RNA binding sites, as the presence of ADP results in a reduction of the equilibrium association constant for NS3h–ssRNA binding. In Figure 6c, we also show the estimated NS3h–ssRNA binding free energies for the apo, ATP-bound, ADP-bound and ADP-Pi-bound complexes, calculated using MM-GBSA for the 16-mer system. Again, we observed a reduction in the affinity for ssRNA in the presence of ATP, relative to the apo complex, and similar binding energies for the ADP, ADP-Pi and ATP-bound complexes. These results indicate at least two energetic states of the NS3h–RNA complex: a tightly bound state with a free NTPase catalytic site, in which the NS3h RNA binding site size is ∼10 nts; and a weakly bound state, in which this size is nearly 7 nts, observed on binding ATP and after hydrolysis. The computed binding free energies for the four modeled complexes (apo, ATP-bound, ADP-Pi-bound and ADP-bound) highlight that the apo NS3h–RNA complex is bound more tightly than the complex with an occupied NTP binding site, which is also consistent with the observed difference in measured equilibrium association constants for the apo- and ADP-bound complexes.

Among increased conformational flexibility, relative subdomain movements are identified

To further probe the interaction between the RNA and ATP binding sites, we asked how the distances between conserved RNA-binding residues on D1 and D2 change during the four stages of the ATP hydrolysis cycle, and how they relate to distances between relevant amino acids (residues from conserved motifs I, III and VI) from the ATP-binding site (Figure 7). Namely, we calculated two inter-subdomain D1–D2 distances at the RNA-binding region (d_{RNA}) and the ATP-binding cleft (d_{ATP}). d_{RNA} is computed as the distance between the centers of mass (COM) of residues Arg 225 and Thr 244 on D1, and Arg 387 and Thr 408 on D2, which are conserved amino acids that anchor the RNA to the NS3h. d_{ATP} is calculated as the COM distance between residues 195, 196, 197 (from motif I), 316 and 317 (from motif III) and residues 458 to 463 (from motif VI) (Figure 7a). Figure 7b shows the 2D density plots for d_{RNA} vs d_{ATP} for the NS3h in its apo, ATP-bound and product-bound stages, in all cases bound to a 16-mer ssRNA.

In the apo state, we observe that the protein explores a wide range of d_{RNA} values (from 12 to 16 Å), as well as d_{ATP} values (from 8 to 15 Å), with greater d_{ATP} distances being more favorable. On binding ATP, although the d_{ATP} values are restrained substantially (clustered around 9 Å), we found two populations in the d_{RNA} dimension, such that the RNA-binding residues are mainly either 13 or 15 Å apart, with the former being substantially more populated. After hydrolysis, we observe that these two populations persist but larger d_{RNA} values become more probable and the flexibility in the d_{ATP} dimension is recovered, as indicated by greater inter-subdomain distances at the ATP-binding level. Interestingly, at this stage of the catalytic cycle (in presence of both products of hydrolysis), when the ATP binding site explores a more open conformation, the RNA binding site necessarily closes and vice versa. In contrast, after the release of the Pi, some flexibility is lost again and a new cluster appears with intermediate values of both distances at the same time.

As mentioned before, the crystals bound to ssRNA show almost no difference between the different stages of the hydrolysis cycle (Figure 7b, black crosses), and the values for d_{RNA} correspond to the cluster recurrently observed at ∼9 Å. Interestingly, for the apo crystal in the absence of RNA, a d_{RNA} length of close to 17 Å is observed (Figure 7b, gray cross). This value is close to the cluster observed in more flexible states.

Asymmetric distribution of contacts between NS3h and ssRNA

To characterize the changes in the RNA binding mode of the DENV NS3h during ATP hydrolysis, we analyzed the number of NS3h–RNA contacts per frame for the simulations of the apo, ATP-bound, ADP-bound and ADP-Pi-bound states, all with the 16-mer oligonucleotide bound (Table 3). Contacts were defined as pairs of residues and nucleotides with centers of mass within 7 Å (Supplementary Figure S7). For the apo complex (i.e. the tightly bound state), the number of contacts is also higher than that for the other stages of the catalytic cycle, and most are formed between the 3′ half of the ssRNA and D1, but there are also many contacts between the 5′ half and D2. In both the ATP-bound and product-bound states, a fraction of the contacts with D1 and D2 are lost, and they are replaced by new contacts with D3, which interacts with the bases of the oligonucleotide but not with the phosphodiester backbone (Figure 3c). This shift corresponds to a change in the orientation of subdomain D3 relative to D1 and D2. In both the ATP and product-bound complexes, we observe an apparent downward movement of D3, which clamps down onto the nucleic acid strand (Supplementary Figure S8). After the release of Pi, the contacts with D3 are lost again; D1 contacts with the 3′ end are recovered, but D2 contacts with the 5′ end are not. These results correlate with the shift toward the 3′ end observed in the RNA binding site after hydrolysis.

We further characterized the interactions between the four NS3h residues from d_{RNA} (Arg 225, Thr 244, Arg 387 and Thr 408), which anchor the RNA to the protein. The crystal structures (PDB IDs 2JLU, 2JLV, 2JLZ and 2JLY) show that the Arg residues interact with the phosphodiester backbone of the oligonucleotide through the backbone amide (NH) and with its positively charged lateral chain; and the threonines

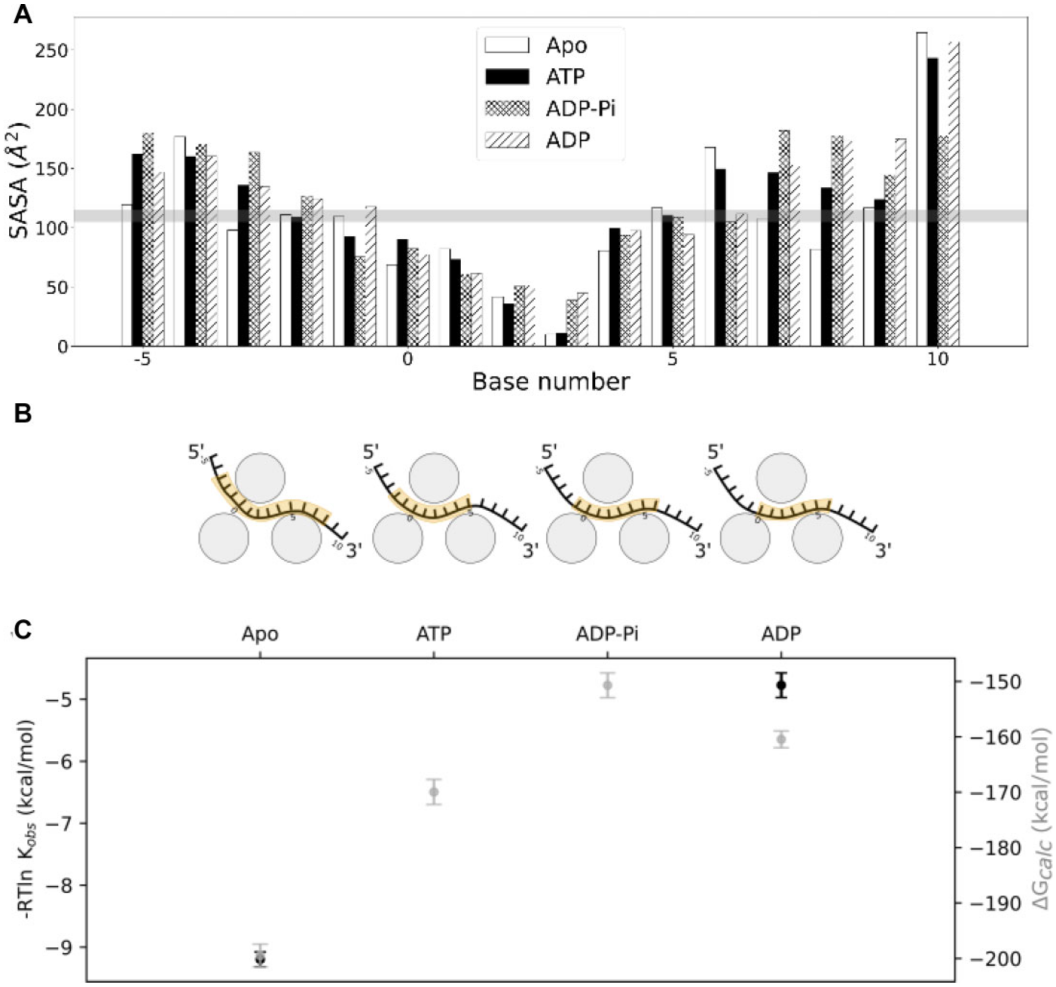

Figure 6. (A) SASA bar plots for the different stages of the catalytic cycle. A gray horizontal line indicates the threshold for determining bases considered to be part of the RNA binding site **(B)** Schematic representation of the NS3h bound to the 16-mer oligonucleotide indicating the ssRNA binding site size in yellow for the apo, ATP-bound, ADP-Pi-bound and ADP-bound states (left to right). 5′ and 3′ ends of the ssRNA are labeled. **(C)** Binding energies for the 16-mer complex in the apo, ATP-bound, ADP-Pi-bound and ADP-bound states shown in gray circles, along with experimental energies calculated from equilibrium constants K_{obs} shown in black circles, with their respective error bars

Table 3. Percentage of contacts per frame formed for each subdomain, for each of the cycle stages, and average number of interactions per frame

Complex	D1 contacts (%)	D2 contacts (%)	D3 contacts (%)	Average contacts per frame
apo	44	28	24	27
ATP	40	26	30	24
ADP-Pi	36	23	36	20
ADP	42	27	27	21

also bind the phosphodiester backbone but through the hydroxyl group of its lateral chain (Figure 7c). When we calculated the percentage of the simulation frames in which the anchors were bound to their corresponding nucleotides and compared those that are present in at least 50% of the simulation frames, we observed that Arg 387 establishes stable interactions with bases B^1 and B^2 only after hydrolysis.

Furthermore, we observed a base flipping in B^{-1} in both ADP-Pi- and ADP-bound complexes, that could also be related to the slight shift and the reduction in the ssRNA binding site size at the 5′ end. Amino acids in the positions of Pro 431 and Leu 429 from the hydrophobic hairpin have been proposed to act as a 'bookend' breaking the stacking of the bases at the RNA 5′ terminus for other flavivirus (33,34) and for other helicases of the DExH ATPase family (35). For the apo and ATP-bound complexes, we observed that B^{-1} was close to the bookend amino acids, but for the ADP-Pi and ADP complexes, this base moves away (Supplementary Table S4). After the chemical step the base stacking between B^0 and B^{-1} is lost because of the B^{-1} flipping. To show this movement, we compared the distance between the center of mass of stacked bases B^1 and B^0, as it is maintained in the four stages of the catalytic cycle, with that of B^0 and B^{-1} and we find that the latter increased for the ADP-Pi- and ADP-bound complexes (Supplementary Figure S10, Supplementary Table S4). At the 3′ end of the ssRNA, we also observed an allosteric effect as

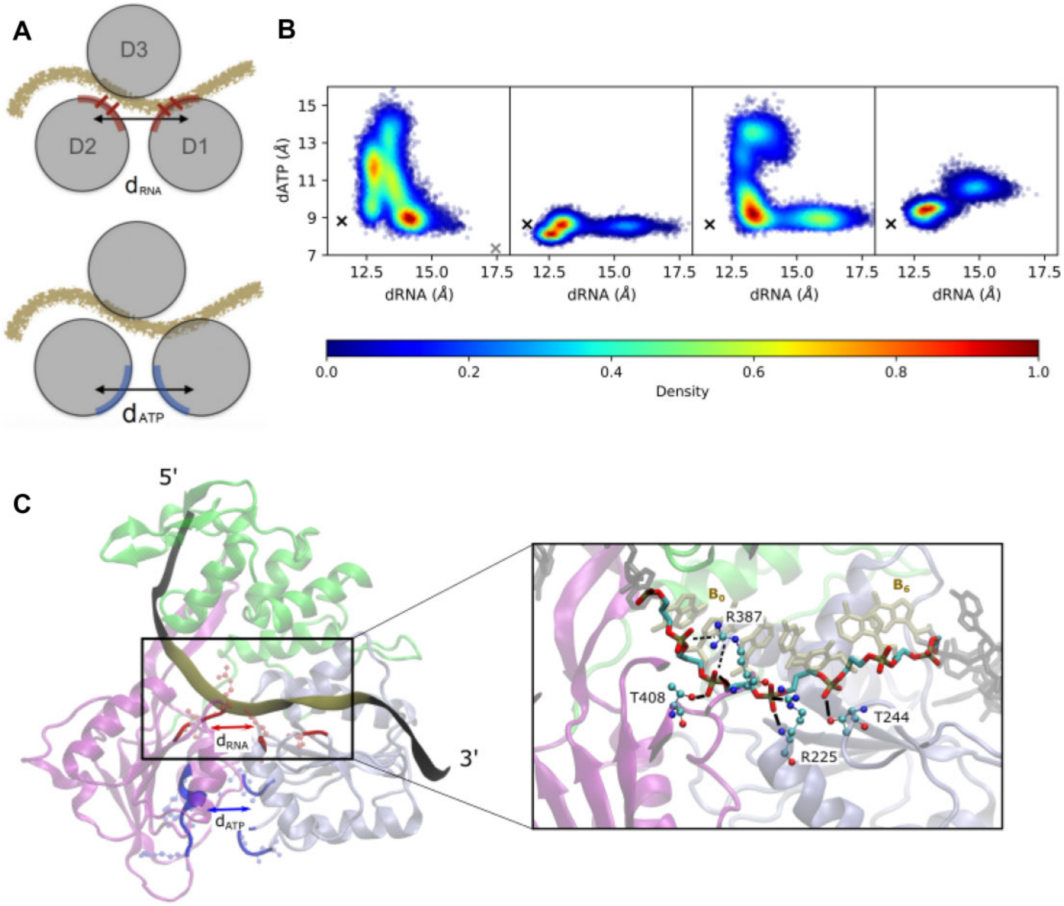

Figure 7. (A) Schematic representation of the protein showing the distances d_{RNA} and d_{ATP}. Subdomains D1, D2 and D3 are labeled. **(B)** Density scatter plot for d_{ATP} vs d_{RNA}. Complexes are, left to right: apo, ATP-bound, ADP-Pi-bound and ADP-bound. The black crosses show the corresponding distances in each crystallographic structure and the gray cross also shows those distances for the protein with no nucleic acid bound. **(C)** The left shows a schematic cartoon representation of the protein (color-coded by subdomain as in Figure 1a). The amino acids involved in the distances d_{RNA} (red) and d_{ATP} (blue) are highlighted. ssRNA is shown as a tan ribbon from bases B^0 to B^6 and as a black ribbon for the rest. 5′ and 3′ ends of the ssRNA are labeled. The right shows the inset zoom in the RNA binding cleft. NS3h residues from d_{RNA} (Arg 225, Thr 244, Arg 387 and Thr 408) are labeled and colored by atom type. The oligonucleotide is shown as sticks, the phosphodiester backbone is colored by atom name and B^0 and B^6 are labeled as a reference. Black lines represent the protein–RNA interactions present in the four complexes and dashed lines represent the protein–RNA interactions that are higher than 50% only after hydrolysis (Supplementary Figure S9, Supplementary Table S3). Snapshot was taken from an ADP-Pi-bound complex simulation.

the NS3h RNA binding loop varies its conformation with the presence and absence of ATP in the catalytic site, which, along with the increased flexibility at the 3′ end, coincides with the reduction of the RNA binding site size.

Discussion

Effect of the presence of extended ssRNA on NS3h conformation

The available crystal structures for the DENV NS3h bound to RNA were obtained using an ssRNA construct of 12 nts. However, in these structures only 7 nts bound to NS3h could be resolved, indicating a larger degree of flexibility of the 3′ and 5′ termini. In our previous MD simulations of the NS3h bound to the 7-mer ssRNA, we further observed a great deal of flexibility at the 3′ terminus of the 7-mer. Importantly, neither the crystal structures nor these MD simulations were able to capture the expected conformational changes due to the occupancy of the NTPase catalytic site. The overall structure was conserved on average, with a notable flexible-rigid-flexible change in the apo, ATP-bound, product-bound stages of the ATP hydrolysis cycle. In this work, we observe that the presence of extended 11-, 16- and 26-nts ssRNA bound to NS3h enhances the flexibility of the protein backbone and that its structure deviates up to 2.5 Å from the crystallographic conformation (Figures 2 and 3).

We attribute the increase in RMSD for the protein bound to longer strands of nucleic acid to the formation of transient protein–RNA interactions, which prompt the exploration of different conformations that were not accessible with shorter RNA oligonucleotides. Regardless of the length of ssRNA, ATP retains its stabilizing effect, as has been reported for other helicases (30), but even the ATP-bound complexes with longer ssRNA are more flexible than those with a shorter oligonucleotide.

The structural deviations observed with the elongation of the RNA strand are predominantly located in the D3 region (Figure 3a and b) and could be due to the interactions between the protein and the ssRNA 5′ terminus (Figure 3c). In particular, the hydrophobic hairpin interacts with the RNA bases at the 5′ end (Figure 3c). In the presence of double-stranded RNA, the hydrophobic hairpin might compete with the displaced strand of the RNA, participating with the unwinding process. This hypothesis would agree with the model proposed by (13) in which the hairpin acts as a wedge, preventing the

RNA from forming the duplex. Druggable pockets near the hairpin may be used for possible inhibition of the helicase activity. It is important to note that in this work our simulations were designed to model the complex relevant in the translocation of NS3h along single-stranded RNA. Future studies including the duplex junction, and even considering structured ssRNA at the 5′ terminus are needed to further probe the allostery of NS3.

RNA binding site size and potential sub-step

One of the objectives of this work was to test the hypothesis that a ssRNA longer than 7 nts is necessary to accurately describe the RNA binding site size of the NS3h. This hypothesis was driven by fluorescence titration experiments of the NS3h with oligonucleotides of different lengths, in which the reported minimum RNA binding site size was 10–11 nts. In this work, we observe an RNA binding site size of ∼10 nts in absence of ATP in both 16- and 26-mer-bound complexes. We further observe that the size of the RNA binding site is reduced by ∼3 nts in the presence of ATP, and this reduction is maintained after hydrolysis before products are released. Although the reduced size of the RNA binding site does not change much after hydrolysis, it is shifted one nucleotide toward the 3′ terminus (Figure 6a). In both 16- and 26-mer apo complexes, the first base of the site is B^{-3}, but on binding ATP, one nucleotide is released and the site starts at B^{-2}. Moreover, the tendency continues post-hydrolysis (first base B^{-1}) and after the release of the first product, Pi (B^0). Taking into account that the NS3h directionality along the RNA is toward the 5′ end and that it is expected to move one base per ATP hydrolysis cycle, one might expect that after the release of the ADP, the first base at the site would be B^{-4}, and so on. The interactions between the NS3h anchors (Arg 225, Thr 244, Arg 387 and Thr 408) and the ssRNA are mostly conserved in the four stages of the catalytic cycle except for Arg 387 (motif IVa), which does not establish stable interactions with any nucleotide in the apo and ATP-bound complexes, but does play an important role in both product-bound stages. Interestingly, the simulations show that the side chain of Arg 387 tends to maintain its interaction with B^1 for longer than with B^2 post-hydrolysis (Supplementary Figure S9, Supplementary Table S3). Thus, it would be reasonable to think that the probability of a step in the 3′-to-5′ direction would be higher than in the opposite direction. Conformational changes in this amino acid side chain have also been reported to be related to a step of NS3h displacement along ssRNA in another computational study of the DENV NS3h (19).

Sufficiently long ssRNA is necessary to describe the allosteric interaction between RNA and ATP binding sites

The decrease in the size of the RNA binding site of the NS3h due to the presence of ATP is consistent with the observed decrease in the binding affinity for RNA due to the presence of ATP, ADP-Pi or ADP in the catalytic site. An observed decrease in the affinity for RNA due to the presence of ATP has also been reported for the HCV NS3h (31,32).

Our results indicate that the allostery between the RNA and ATP binding sites is influenced by the length of the oligonucleotide: without a sufficiently long oligonucleotide such allostery is not observed. This result indicates that the transient protein–RNA interactions play a critical role in the allostery between the RNA and ATP binding sites. The increased affinity observed for longer ssRNA oligonucleotides is an example of a phenomenon described as the Coulombic end effect (CEE) (36–39), caused by the strong axial dependence of the surface electrostatic potential of nucleic acids, which leads to a transition between oligoelectrolyte to polyelectrolyte behavior of the nucleic acid in the range of ssRNA lengths examined here. In this context, considering the charge of the NS3h and the characteristic CEE length of 9 nts (38), we would expect that the binding free energy would cease to be length dependent at ∼23 nts. Of course, this prediction is for a model that does not take into consideration the association of multiple NS3h molecules, which is a separate effect that has also been reported to cause a length dependence of the observed binding affinity of NS3h to ssRNA in solution (15).

The DENV genome (∼11 kb) is much longer than the ssRNA lengths studied here; however this genomic RNA is in large part structured on itself and in complex with viral and host RNA binding proteins, likely leaving much smaller stretches of ssRNA exposed during the viral life cycle (40). Furthermore, small RNA fragments of 15 to 30 nts are known to be present in mammalian host cells and the distribution of these lengths has been shown to be affected by viral infection (41). We are thus confident that an understanding of the length-dependence of the interaction between NS3h and ssRNA is a critical aspect in future drug discovery efforts, in particular in the design of allosteric inhibitors that may leverage novel pockets and conformational changes in the protein structure.

Changes in transient protein–RNA interactions during ATP hydrolysis

The analysis of protein–RNA contacts (Table 3) reveals that to a large extent, the reduced affinity in the ATP- and product-bound complexes can be attributed to a loss of interactions between the 3′ half of ssRNA and subdomain D1. Interestingly, although the total number of contacts with the 5′ half of the ssRNA is approximately constant in all four stages, there is a notable shift in the fraction of the interactions from D2 to D3. Thus, the RNA interactions with the two RecA-like subdomains are to a large extent replaced by new interactions with D3 on binding of ATP and even after hydrolysis. After release of Pi, these new interactions with D3 are lost again. The correlation between the change in the percentage of contacts with D3 and the estimated binding free energy suggests that the electrostatic interaction between D1 and D2 with the phosphodiester backbone of the oligonucleotide would give the complex a lower binding energy compared to the interactions between the bases of the oligonucleotide and D3.

When we further take into account the distance between key RNA-binding residues (d_{RNA}) or key ATP-binding residues (d_{ATP}) on the two RecA-like subdomains D1 and D2, we observe a clear population shift in terms of both separations during the ATP hydrolysis cycle. In terms of the separation of RNA-binding residues, roughly two populations are observed at ∼14.5 and 12.5 Å, ‘relaxed’ and ‘tense’, respectively. Interestingly, variations in the d_{RNA} distance are characteristic of the difference between the crystal structures of the DENV NS3h obtained in the presence and absence of ssRNA, with larger values being observed in the absence of ssRNA (see crosses in Figure 7b). In the apo state, the relaxed RNA binding mode is more favorable than the tense mode, whereas the opposite is observed for both the ATP- and ADP-Pi-bound states, and the physical gap between the two states widens slightly in these cases cases as well. Similarly, a relaxed and tense conformation of the ATP binding site can be identified in the apo state, with the relaxed state being more favorable. On binding of ATP, these residues are exclusively in the tense state, characterized by lower d_{ATP} distances, and on hydrolysis of ATP, the relaxed state is explored once more. It is interesting to note that although the tense RNA binding mode is favored in presence of ATP, the relaxed mode characterized by larger d_{RNA} distances is still explored. Mechanistically, this could be interpreted as the protein 'loosening its grip' on the ssRNA (Figure 5a) on tightening its grip on ATP, thus permitting the exploration of multiple binding modes along the nucleic acid.

Configurational entropy as a driving force for unidirectional translocation

The D3 subdomain shows an increased number of contacts with the ssRNA for the ATP- and ADP-Pi-bound complexes, which corresponds to an apparent downward movement of D3 toward the ssRNA in the presence of ATP and products. These additional interactions could also help in biasing the directionality of the movement toward the 5′ terminus, which is where it has key contacts.

The per-nt SASA analysis of the different RNA oligonucleotides considered highlights the general tendency of flexible ssRNA termini, with a stable, highly interacting core. On taking a closer look at the per-nt RMSF values for the apo, ATP-bound and product-bound states (Supplementary Figure S5), we can further identify a change in the asymmetrical aspect of these fluctuations. In the apo system, the 3′ terminus (right side) is stabilized, and the highest RMSF values are located at the 5′ terminus (left side). On binding of ATP, however, the 3′ terminus becomes as flexible as the 5′ terminus, and in the presence of the products ADP and Pi, the flexibility of the ssRNA is localized at the 3′ terminus. After release of Pi, the flexibility of the 5′ terminus is recovered for the most part. This change in the asymmetry of the flexibility of nucleotides toward the 3′ and 5′ termini, in addition to the increased mobility of the 3′ terminus on hydrolysis of ATP—that is likely associated with a large entropic cost for advancing in the 3′ direction—are consistent with the 3′-to-5′ directionality of the helicase. The stabilization of the 5′ terminus exclusively in the presence of ADP-Pi suggests that a step in the 5′ direction would be the least costly before or concomitant with Pi release.

Conclusion

The use of atomistic models and MD simulations have become integral components in drug discovery pipelines. We and others have simulated the NS3h–ssRNA complex as it has been crystallized, with a 7-nts ssRNA fragment bound, to elucidate the allosteric networks that connect the NTPase active site to the RNA binding site. Contrary to our expectations, the simulations did not indicate substantial changes in the NS3h–ssRNA interaction due to the presence of ATP or products of hydrolysis (17). Here, we have established that the length of the bound ssRNA fragment is critical in accurately capturing this allostery, in which the presence of ATP, ADP or products of hydrolysis result in a more weakly bound NS3h–ssRNA complex than in the apo state. These results are of direct implication in the interpretation of *in vitro* studies of the NS3h with ssRNA as well as in future computational drug discovery efforts for NS3 inhibitors.

Data availability

The data underlying this article will be shared on reasonable request to the corresponding author.

Supplementary data

Supplementary Data are available at NAR Online.

Acknowledgements

We would like to acknowledge the CeCAR supercomputing facility and INQUIMAE cluster at the Faculty of Exact and Natural Sciences of the University of Buenos Aires. Amrein, F. and Sarto, C. are CONICET doctoral fellows.

Funding

Agencia Nacional de Promoción Científica y Tecnológica (Grant / Award Number: ANPCyT-PICT 2020-3445, PICT-2021-GRF-TI-00403, PICT-2021-I-INVI-00854). Funding for open access charge: Agencia Nacional de Promoción Científica y Tecnológica (Grant / Award Number: ANPCyT-PICT 2020-3445).

Conflict of interest statement

None declared.

References

1. Bhatt,S., Gething,P.W., Brady,O.J., Messina,J.P., Farlow,A.W., Moyes,C.L., Drake,J.M., Brownstein,J.S., Hoen,A.G., Sankoh,O., *et al.* (2013) The global distribution and burden of dengue. *Nature*, **496**, 504.
2. Park,J., Kim,J. and Jang,YS. (2022) Current status and perspectives on vaccine development against Dengue virus infection. *J. Microbiol.*, **60**, 247–254.
3. Lescar,J., Luo,D., Xu,T., Sampath,A., Lim,S.P., Canard,B. and Vasudevan,S.G. (2008) Towards the design of antiviral inhibitors against flaviviruses: the case for the multifunctional NS3 protein from Dengue virus as a target. *Antivir. Res.*, **80**, 94–101.
4. Matusan,A.E., Pryor,M.J., Davidson,A.D. and Wright,P.J. (2001) Mutagenesis of the Dengue virus type 2 NS3 protein within and outside helicase motifs: effects on enzyme activity and virus replication. *J. Virol.*, **75**, 9633–9643.
5. Heaton,N.S., Perera,R., Berger,K.L., Khadka,S., Lacount,D.J., Kuhn,R.J. and Randall,G. (2010) Dengue virus nonstructural protein 3 redistributes fatty acid synthase to sites of viral replication and increases cellular fatty acid synthesis. *Proc. Natl Acad. Sci. USA*, **107**, 17345–17350.
6. Perera,R. and Kuhn,R.J. (2008) Structural proteomics of Dengue virus. *Curr. Opin. Microbiol.*, **11**, 369–377.
7. Li,H., Clum,S., You,S., Ebner,K.E. and Padmanabhan,R. (1999) The serine protease and RNA-stimulated nucleoside triphosphatase and RNA helicase functional domains of Dengue virus type 2 NS3 converge within a region of 20 amino acids. *J. Virol.*, **73**, 3108–3116.
8. Incicco,J.J., Gebhard,L.G., Gonzalez-Lebrero,R.M., Gamarnik,A.V. and Kaufman,S.B. (2013) Steady-state NTPase activity of Dengue virus NS3: number of catalytic sites, nucleotide specificity and activation by ssRNA. *PLoS ONE*, **8**, e58508.

9. Gebhard,L.G., Kaufman,S.B. and Gamarnik,A.V. (2012) Novel ATP-independent RNA annealing activity of the Dengue virus NS3 helicase. *PLoS ONE*, **7**, e36244.
10. Benarroch,D., Selisko,B., Locatelli,G.A., Maga,G., Romette,J.-L. and Canard,B. (2004) The RNA helicase, nucleotide 5-triphosphatase, and RNA 5-triphosphatase activities of Dengue virus protein NS3 are Mg2 +-dependent and require a functional Walker B motif in the helicase catalytic core. *Virology*, **328**, 208–218.
11. Xu,T., Sampath,A., Chao,A., Wen,D., Nanao,M., Chene,P., Vasudevan,S.G. and Lescar,J. (2005) Structure of the Dengue virus helicase/nucleoside triphosphatase catalytic domain at a resolution of 2.4 Å. *J. Virol.*, **79**, 10278–10288.
12. Li,H., Clum,S., You,S., Ebner,K.E. and Padmanabhan,R. (1999) The serine protease and RNA-stimulated nucleoside triphosphatase and RNA helicase functional domains of Dengue virus type 2 NS3 converge within a region of 20 amino acids. *J. Virol.*, **73**, 3108–3116.
13. Luo,D., Xu,T., Watson,R.P., Scherer-Becker,D., Sampath,A., Jahnke,W., Yeong,S.S., Wang,C.H., Lim,S.P., Strongin,A., Vasudevan,S.G. and Lescar,J. (2008) Insights into RNA unwinding and ATP hydrolysis by the flavivirus NS3 protein.. *EMBO J.*, **27**, 3209–3219.
14. Swarbrick,C.M.D., Basavannacharya,C., Chan,K.W.K., Chan,S.A., Singh,D., Wei,N., Phoo,W.W., Luo,D., Lescar,J. and Vasudevan,S.G. (2017) NS3 helicase from Dengue virus specifically recognizes viral RNA sequence to ensure optimal replication. *Nucleic Acids Res.*, **45**, 12904–12920.
15. Gebhard,L.G., Incicco,J.J., Smal,C., Gallo,M., Gamarnik,A.V. and Kaufman,S.B. (2014) Monomeric nature of Dengue virus NS3 helicase and thermodynamic analysis of the interaction with single-stranded RNA.. *Nucleic Acids Res.*, **42**, 11668–11686.
16. Todd,C.A., Anderson,R., Fedorova,O., Pyle,A.M., Wang,R., Liu,X., Brendza,K.M. and Somoza,J.R. (2011) Visualizing ATP-dependent RNA translocation by the NS3 helicase from HCV. *J. Mol. Biol.*, **405**, 1139–1153.
17. Sarto,C., Kaufman,S.B., Estrin,D.A. and Arrar,M. (2020) Nucleotide-dependent dynamics of the Dengue NS3 helicase.. *Biochim. Biophys. Acta Proteins Proteom.*, **1868**, 140441.
18. Adler,N.S., Cababie,L.A., Sarto,C., Cavasotto,C.N., Gebhard,L.G., Estrin,D.A., Gamarnik,A.V., Arrar,M. and Kaufman,S.B. (2022) Insights into the product release mechanism of Dengue virus NS3 helicase. *Nucleic Acids Res.*, **50**, 6968–6979.
19. Davidson,R.B., Hendrix,J., Geiss,B.J. and McCullagh,M. (2018) Allostery in the Dengue virus NS3 helicase: insights into the NTPase cycle from molecular simulations. *PLoS Comput. Biol.*, **14**, e1006103.
20. Du Pont,K.E., Davidson,R.B., McCullagh,M. and Geiss,B.J. (2020) Motif V regulates energy transduction between the flavivirus NS3 ATPase and RNA-binding cleft. *J. Biol. Chem.*, **295**, 1551–1564.
21. Humphrey,W., Dalke,A. and Schulten,K. (1996) VMD - visual molecular dynamics. *J. Molec. Graphics*, **14**, 33–38.
22. Meagher,K.L., Redman,L.T. and Carlson,H.A. (2003) Development of polyphosphate parameters for use with the AMBER force field. *J. Comput. Chem.*, **24**, 1016–1025.
23. Maier,J.A., Martinez,C., Kasavajhala,K., Wickstrom,L., Hauser,K.E. and Simmerling,C. (2015) ff14SB: improving the accuracy of protein side chain and backbone parameters from ff99SB. *J. Chem. Theor. Comput.*, **11**, 3696–3713.
24. Aytenfisu,A.H., Spasic,A., Grossfield,A., Stern,H.A. and Mathews,D.H. (2017) Revised RNA dihedral parameters for the Amber force field improve RNA molecular dynamics. *J. Chem. Theor. Comput.*, **13**, 900–915.
25. Case,D.A., Darden,T.A., Cheatham,T.E. III, Simmerling,C.L., Wang,J., Duke,R.E., Luo,R., Walker,R.C., Zhang,W., Merz,K.M., *et al.* (2010) *Amber 16*. University of California, San Francisco.
26. Jorgensen,W.L., Chandrasekhar,J., Madura,J.D., Impey,R.W. and Klein,M.L. (1983) Comparison of simple potential functions for simulating liquid water. *J. Chem. Phys.*, **79**, 926–935.
27. Onufrie,A., Bashford,D. and Case,D.A. (2004) Exploring protein native states and large-scale conformational changes with a modified generalized Born model. *Proteins*, **55**, 383–394.
28. Kinney,R.M., Butrapet,S., Chang,G.J., Tsuchiya,K.R., Roehrig,J.T., Bhamarapravati,N. and Gubler,D.J. (1997) Construction of infectious cDNA clones for dengue 2 virus: strain 16681 and its attenuated vaccine derivative, strain PDK-53. *Virology*, **230**, 300–308.
29. Borowski,P., Niebuhr,A., Mueller,O., Bretner,M., Felczak,K., Kulikowski,T. and Schmitz,H. (2001) Purification and characterization of West Nile virus nucleoside triphosphatase (NTPase)/helicase: evidence for dissociation of the NTPase and helicase activities of the enzyme. *J. Virol.*, **75**, 3220–3229.
30. Pérez-Villa,A., Darvas,M. and Bussi,G. (2015) ATP dependent NS3 helicase interaction with RNA: insights from molecular simulations. *Nucleic Acids Res.*, **43**, 8725–8734.
31. Levin,M.K., Gurjar,M.M. and Patel,S.S. (2003) ATP binding modulates the nucleic acid affinity of hepatitis C virus helicase. *J. Biol. Chem.*, **278**, 23311–23316.
32. Porter,D.J. and Preugschat,F. (2000) Strand-separating activity of hepatitis C virus helicase in the absence of ATP. *Biochemistry*, **39**, 5166–5173.
33. Gao,X., Zhu,K., Wojdyla,J.A., Chen,P., Qin,B., Li,Z., Wang,M. and Cui,S. (2020) Crystal structure of the NS3-like helicase from Alongshan virus. *IUCrJ.*, **7**, 375–382.
34. Gu,M. and Rice,C.M. (2009) Three conformational snapshots of the hepatitis C virus NS3 helicase reveal a ratchet translocation mechanism. *Proc. Natl Acad. Sci. USA*, **107**, 521–528.
35. He,Y., Staley,J.P., Andersen,G.R. and Nielsen,K.H. (2017) Structure of the DEAH/RHA ATPase Prp43p bound to RNA implicates a pair of hairpins and motif Va in translocation along RNA. *RNA*, **23**, 1110–1124.
36. Zhang,W., Ni,H., Capp,M.W., Anderson,C.F., Lohman,T.M. and Thomas Record,M. Jr (1999) The importance of Coulombic end effects: experimental characterization of the Effects of oligonucleotide flanking charges on the strength and salt dependence of oligocation (L8) binding to single-stranded DNA oligomers. *Biophys. J.*, **76**, 1008–1017.
37. Zhang,W., Bond,J.P., Anderson,C.F., Lohman,T.M. and Thomas Record,M. Jr (1996) Large electrostatic differences in the binding thermodynamics of a cationic peptide to oligomeric and polymeric DNA. *Proc. Natl Acad. Sci. USA*, **93**, 2511–2516.
38. Shkel,I.A., Ballin,J.D. and Thomas Record,M. Jr (2006) Interactions of cationic ligands and proteins with small nucleic acids: analytic treatment of the large coulombic end effect on binding free energy as a function of salt concentration. *Biochemistry*, **45**, 8411–8426.
39. Olmsted,M.C., Anderson,C.F. and Thomas Record,M. Jr (1989) Monte Carlo description of oligoelectrolyte properties of DNA oligomers: range of the end effect and the approach of molecular and thermodynamic properties to the polyelectrolyte limits. *Proc. Natl Acad. Sci. USA*, **86**, 7766–7770.
40. Chambers,T.J., Hahn,C.S., Galler,R. and Rice,C.M. (1990) Flavivirus genome organization, expression, and replication. *Ann. Rev. Microbiol.*, **44**, 649–688.
41. Jackowiak,P., Hojka-Osinska,A., Philips,A., Zmienko,A., Budzko,L., Maillard,P. and Figlerowicz,M. (2017) Small RNA fragments derived from multiple RNA classes–the missing element of multi-omics characteristics of the hepatitis C virus cell culture model. *BMC Genomics*, **18**, 1–21.

Received: March 9, 2023. **Revised:** August 20, 2023. **Editorial Decision:** September 13, 2023. **Accepted:** September 19, 2023